Nanoscale Advances

ROYAL SOCIETY OF CHEMISTRY

PAPER

View Article Online
View Journal | View Issue

Cite this: *Nanoscale Adv.*, 2021, **3**, 5062

Pt_3Sn nanoparticles enriched with SnO_2/Pt_3Sn interfaces for highly efficient alcohol electrooxidation†

Zichen Wang,[a] Liang Wang,[a] Wangbin Zhu,[a] Tang Zeng,[a] Wei Wu,[a] Zhao Lei,[a] Yangyang Tan,[a] Haifeng Lv *[bc] and Niancai Cheng *[a]

Received 28th April 2021
Accepted 2nd July 2021

DOI: 10.1039/d1na00314c

rsc.li/nanoscale-advances

Pt_3Sn nanoparticles (NPs) enriched with Pt_3Sn/ultra-small SnO_2 interfaces (Pt_3Sn@u-SnO_2/NG) were synthesized through a thermal treatment of Pt_2Sn/NG in a H_2 atmosphere, followed by annealing under H_2 and air conditions. The unique structure of Pt_3Sn NPs enriched with Pt_3Sn/SnO_2 interfaces was observed on the Pt_3Sn@u-SnO_2/NG catalyst based on HRTEM. The optimized Pt_3Sn@u-SnO_2/NG catalyst achieves high catalytic activity with an ethanol oxidation reaction (EOR) activity of 366 mA mg_{Pt}^{-1} and a methanol oxidation reaction (MOR) activity of 503 mA mg_{Pt}^{-1} at the potential of 0.7 V, which are eight-fold and five-fold higher than those for the commercial Pt/C catalyst (44 and 99 mA mg_{Pt}^{-1}, respectively). The Pt_3Sn@u-SnO_2/NG catalyst is found to be 3 times more stable and have higher CO tolerance than Pt/C. The outstanding performance of the Pt_3Sn@u-SnO_2/NG catalyst should be ascribed to the synergetic effect induced by the unique structure of Pt_3Sn NPs enriched with Pt_3Sn/SnO_2 interfaces. The synergetic effect between Pt_3Sn NPs and ultra-small SnO_2 increases the performance for alcohol oxidation because the Sn in both Pt_3Sn and SnO_2 favors the removal of CO_{ads} on the nearby Pt by providing OH_{ads} species at low potentials. The present work suggests that the Pt_3Sn@u-SnO_2 is indeed a unique kind of efficient electrocatalyst for alcohol electrooxidation.

1. Introduction

During the past few decades, direct alcohol fuel cells (DAFCs) have emerged as an attractive alternative energy technology for portable electronics and vehicles due to their high energy density, low pollutant emission and easy storage and transportation.[1–3] Pt/C catalysts are the most popular electrocatalysts to accelerate the kinetics of the methanol oxidation reaction (MOR) and ethanol oxidation reaction (EOR) at the anode in DAFCs.[4–6] However, the practical adoption of DAFCs is limited by the high cost, low activities and poor durability of Pt/C catalysts.[6,7] Furthermore, Pt is highly susceptible to being poisoned by intermediates such as CO, which easily adsorb on Pt and block the active sites of Pt catalysts, thus leading to the deactivation of Pt NPs.[8,9]

To address the above issues, Pt alloying with other transition metals is an effective strategy to promote the oxidation of methanol/ethanol.[2,10–12] Different bimetallic PtM (M = Ru, Rh, Co, Ni, Fe, Sn) catalysts with different structures have been explored to improve the Pt activity and stability towards oxidation of methanol/ethanol.[13–19] The improvement in the performance of Pt alloys is attributed to a bifunctional and/or electronic effect of transition metals on Pt.[20–22] Among these Pt alloys, Pt alloyed with Sn has received considerable attention for alcohol oxidation mainly due to its superior performance with high CO-poisoning tolerance.[23–26] For example, compared with pure nanowires, ultrathin Pt_xSn_{1-x} nanowires were found to not only achieve superior activity and stability towards the MOR and EOR, but also exhibit much lower onset potentials.[27–29] Furthermore, Pt_3Sn NPs are reported to have higher EOR activity than PtSn NPs.[30]

The design of interfacial Pt–metal oxide structures in DAFC anode catalytic systems is believed to be another effective strategy.[31–34] The interfacial Pt–metal oxide structures not only improve the stability resulting from the strong metal–support interaction (SMSI) effect, but also improve the Pt activity through the bifunctional mechanism, wherein metal oxides provide adsorbed hydroxyl groups for adjacent Pt active sites to facilitate the oxidation and removal of the reaction intermediates (*e.g.*, CH_x and CO) at a lower potential and thus improve the Pt activity towards the MOR and EOR.[35] For example, SnO_2 NPs were widely used to provide hydroxyl groups for helping the removal of adsorbed CO on the surface of Pt, leading to

[a]*College of Materials Science and Engineering, Fuzhou University, Fuzhou 350108, Fujian, China. E-mail: niancaicheng@fzu.edu.cn*

[b]*PEM Fuel Cell Catalyst Research and Development Center, Shenzhen, Guangdong, 518057, China*

[c]*Materials Science Division, Argonne National Laboratory, Argonne, IL 60439, USA. E-mail: lvhaifenganl@gmail.com*

† Electronic supplementary information (ESI) available. See DOI: 10.1039/d1na00314c

improved electrocatalytic performance for methanol/ethanol oxidation.[36,37] Recently, Cheng *et al.*[38] annealed Pt–Sn on N-doped graphene under air conditions to ensure that each generated Pt_3Sn NP is in close contact with one or more SnO_2 NPs, resulting in high activity towards the MOR and EOR due to the formation of the interfacial Pt_3Sn–SnO_2 structures. However, designing enough interfacial Pt–metal oxides around Pt-based catalysts is still a big challenge.

In this work, we developed highly active and stable Pt_3Sn NPs enriched with SnO_2/Pt_3Sn interfaces through surface restructuring in Pt_2Sn NPs under H_2 and air conditions. As shown in Scheme 1, Pt_2Sn/NG catalysts were firstly obtained by deposition of Pt_2Sn NPs on nitrogen-doped graphene (NG) using the polyol method[39] with the nominal Pt/Sn atomic ratio of 2 : 1. The Pt_3Sn NPs enriched with SnO_2/Pt_3Sn interfaces on the NG (Pt_3Sn@u-SnO_2/NG) were achieved through thermal treatment of Pt_2Sn/NG in a H_2 atmosphere, followed by annealing under air conditions. Pt_3Sn@u-SnO_2/NG catalysts display superior activity and excellent stability for the EOR and MOR.

2. Results and discussion

2.1 Structure of the catalyst

X-ray diffraction (XRD) was firstly applied to monitor the transformation of Pt_2Sn/NG to Pt_3Sn@u-SnO_2/NG. Three broad peaks centered at 38.9°, 45.2° and 66.5° were detected for the Pt_2Sn/NG catalyst (Fig. 1), owing to the reflections of (111), (200) and (220) planes of Pt NPs with a face-centered cubic (fcc) structure, respectively.[40] After treatment of Pt_2Sn/NG in H_2/N_2 at 300 °C for 1 h, stronger and sharper diffraction peaks appear, which indicates the formation of a large particle size in the Pt_2Sn–H/NG catalyst. Compared with commercial Pt/C and Pt_2Sn–H/NG catalysts, it is obvious that diffraction peaks in the Pt_3Sn@u-SnO_2/NG catalyst negatively shift to 38.8°, 45.5° and 66.1°, which are close to (111), (200) and (220) planes of the Pt_3Sn NPs (PDF# 35-1360). Furthermore, small and broadened diffraction peaks of SnO_2 were observed, which demonstrate the ultra-small feature of SnO_2 NPs. A strong diffraction peak at about *ca.* 25.5° was observed, originating from the (002) reflections of NG.

Transmission electron microscopy (TEM) was further performed to investigate the structural evolution upon the thermal treatment of the Pt_2Sn/NG sample. Fig. S1† shows that Pt_2Sn NPs with 2–4 nm in diameter were highly dispersed on NG. A larger particle size of Pt_2Sn NPs is found to be formed after treatment of Pt_2Sn/NG in H_2/N_2 at 300 °C for 1 h as shown in Fig. S2.† After contiguous annealing of the Pt_2Sn–H/NG sample in air at 300 °C for 1 h, the interplanar spacings were measured to be 0.200 and 0.231 nm, as shown in Fig. 2b, corresponding to the spacings between the (200) and (111) facets of fcc Pt_3Sn, respectively. The Pt_3Sn formation in Pt_3Sn@u-SnO_2/NG was further displayed by the selected diffraction pattern as shown in Fig. S3.† In addition to the typical (111) and (200) planes, we found Pt_3Sn specific superlattice diffraction rings with diameters of 11.17 nm^{-1}, 14.08 nm^{-1} and 16.65 nm^{-1}. The corresponding crystal plane spacing was 0.179 nm, 0.142 nm and 0.120 nm, respectively, which are attributed to (210), (220) and

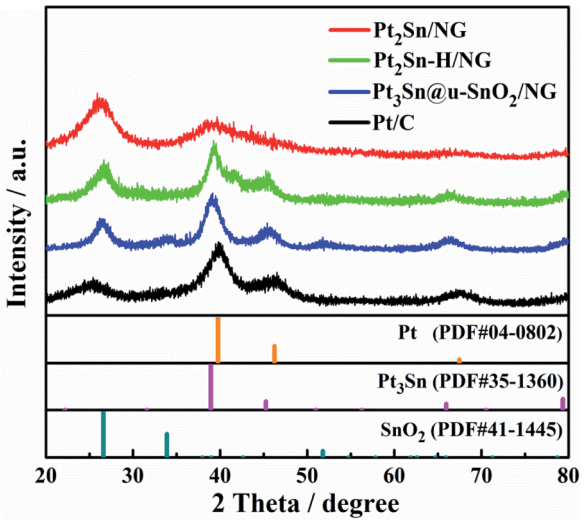

Fig. 1 XRD patterns of the Pt_2Sn/NG, Pt_2Sn–H/NG, Pt_3Sn@u-SnO_2/NG and Pt/C catalysts.

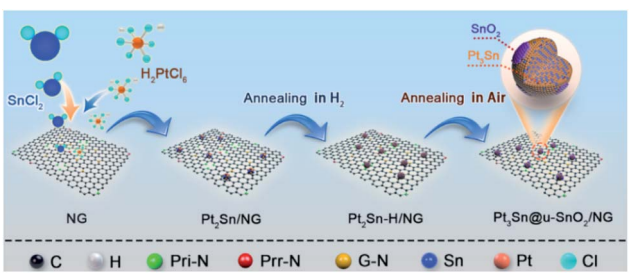

Scheme 1 Schematic diagram of the synthesis of Pt_3Sn@u-SnO_2 on N-doped graphene.

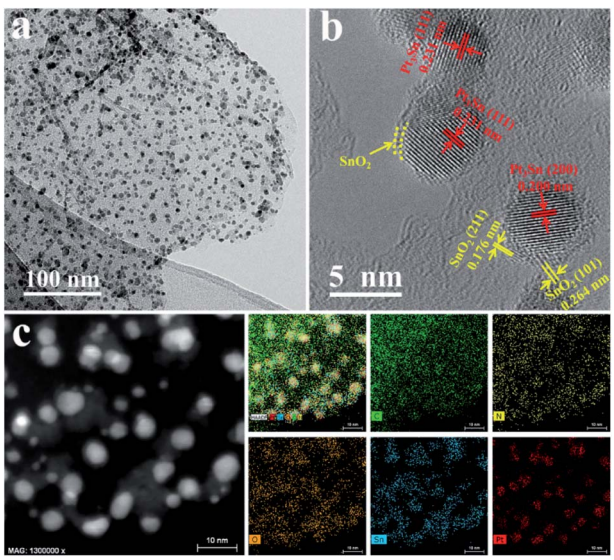

Fig. 2 (a) TEM and (b) HRTEM images of the Pt_3Sn@u-SnO_2/NG catalyst. (c) STEM image and the corresponding elemental maps of C, N, O, Sn and Pt.

(311) of Pt_3Sn, respectively. More importantly, ultra-small SnO_2 NPs on the Pt_3Sn NPs were found, in accordance with the analysis of XRD. This result suggests the formation of the interfacial Pt_3Sn–SnO_2 structures on Pt_3Sn NPs through surface restructuring in Pt_2Sn NPs under air conditions. Pt-based catalysts enriched with Pt/metal oxides have proved to increase the EOR due to the enhanced C–C bond cleavage.[41] The elemental mapping images as shown in Fig. 2c also indicate that the Sn element is distributed around the Pt_3Sn NPs, which confirms that there are abundant ultra-small SnO_2 NPs around the Pt_3Sn NPs.

X-ray photoelectron spectroscopy (XPS) was carried out to observe the effect of thermal treatment in H_2 and air on the surface properties of the Pt_2Sn/NG sample shown in Fig. 3. The high resolution XPS spectrum of Pt_2Sn/NG in the Pt 4f region (Fig. 3b) clearly shows the binding energies of Pt $4f_{5/2}$ at 74.77 eV and Pt $4f_{7/2}$ at 71.49 eV, which are a little lower than those of the Pt/C catalyst (75.10 and 71.76 eV). After thermal treatment of the Pt_2Sn/NG sample in H_2, the binding energies of Pt $4f_{5/2}$ and Pt $4f_{7/2}$ for the Pt_2Sn–H/NG sample were negatively shifted to 74.59 eV and 71.23 eV. The thermal treatment in H_2 changed the crystal structure and degree of ordering of the alloy, which leads to the tuning of the Pt surface electronic structure and thus the downshift of Pt 4f.[42] After annealing of the Pt_2Sn–H/NG sample in air, the binding energies of Pt $4f_{5/2}$ and Pt $4f_{7/2}$ for the Pt_3Sn@u-SnO_2/NG sample positively shift to 74.61 eV and 71.32 eV. The deconvoluted Pt 4f spectrum of the Pt_3Sn@u-SnO_2/NG sample as shown in Fig. 3b indicates that two doublets are located at binding energies of 71.32/74.61 eV and 72.50/75.90 eV, corresponding to metal Pt and the bivalent Pt ion, respectively. The binding energies of Pt $4f_{5/2}$ and Pt $4f_{7/2}$ for the other samples are summarized in Table S2.† Fig. 3c shows the deconvoluted Sn 3d spectra of Pt_2Sn/NG, Pt_2Sn–H/NG and Pt_3Sn@u-SnO_2/NG samples. The main two bands located at about 486.93/495.34 eV and 485.51/494.04 eV were observed for these three samples (Table S3†), which should be attributed to Sn(II/IV) and Sn(0). As given in Table S4,† the Sn(0) content in Pt_2Sn–H/NG is higher than that of Pt_2Sn/NG, which is mainly due to the change in the crystal structure and degree of ordering of the alloy.[43] Compared with Pt_2Sn–H/NG, the Pt_3Sn@u-SnO_2/NG sample has a lower content of Sn(0) due to the formation of SnO_2. There is no significant change observed for N configurations and content in NG after the thermal treatment at 300 °C in H_2 and air atmospheres (Fig. 3d).

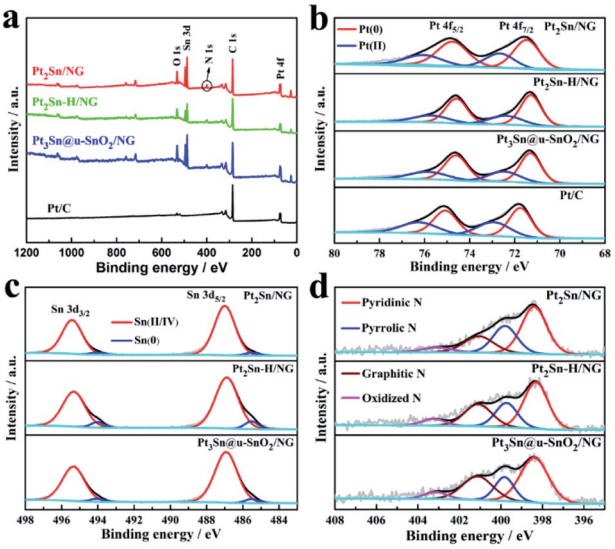

Fig. 3 (a) XPS survey spectra of Pt_2Sn/NG, Pt_2Sn–H/NG, Pt_3Sn@u-SnO_2/NG and Pt/C catalysts. (b) High-resolution Pt 4f spectra of Pt_2Sn/NG, Pt_2Sn–H/NG, Pt_3Sn@u-SnO_2/NG and Pt/C catalysts. High-resolution (c) Sn 3d and (d) N 1s spectra of Pt_2Sn/NG, Pt_2Sn–H/NG and Pt_3Sn@u-SnO_2/NG catalysts.

2.2 Evaluation of electrochemical activity

The cyclic voltammograms (CVs) of the as-prepared Pt_3Sn@u-SnO_2/NG were recorded prior to evaluating its EOR activity. The CVs of Pt_3Sn@u-SnO_2/NG, Pt_2Sn–H/NG and Pt_2Sn/NG as shown in Fig. S4a† showed different adsorption/desorption peaks compared with the Pt/C catalyst, which arise from the insertion of Sn into the Pt lattice.[42] The EOR performance of our samples was characterized as shown in Fig. 4 and the current densities were normalized with respect to the Pt loading. It is observed from polarization curves for ethanol oxidation in Fig. 4a that the peak EOR current densities of different catalysts decrease in the

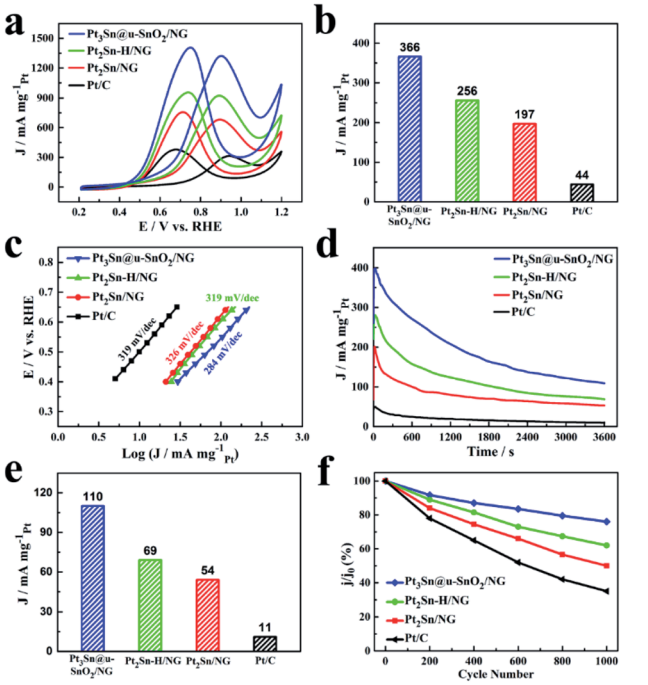

Fig. 4 (a) CV curves of different catalysts in 0.5 M H_2SO_4 + 1 M CH_3CH_2OH solution with a sweep rate of 50 mV s^{-1}. (b) The current density of different catalysts at 0.7 V in 0.5 M H_2SO_4 + 1 M CH_3CH_2OH solution. (c) Corresponding Tafel plots for the EOR on different catalysts. (d) Chronoamperometric curves of t of different catalysts in N_2-saturated 0.5 M H_2SO_4 + 1 M CH_3CH_2OH solution at constant voltage 0.7 V for 3600 s. (e) The current density at 0.7 V at 3600 s for different catalysts obtained from Fig. 4d. (f) Changes of peak current densities of the EOR during potential cycling of different catalysts.

order of Pt_3Sn@u-SnO_2/NG > Pt_2Sn–H/NG > Pt_2Sn/NG > Pt/C (30%, JM). We also find that the onset potential of the EOR on different catalysts follows the same trend as shown in Fig. S4.† More importantly, Pt_3Sn@u-SnO_2/NG shows higher EOR activity compared with the other samples during 0.45–0.7 V *vs.* RHE (Fig. S5†) for the practical applications of direct ethanol fuel cells (DEFCs).[44] The mass activity of 366 mA mg_{Pt}^{-1} was achieved on Pt_3Sn@u-SnO_2/NG at 0.7 V (Fig. 4b), which is 1.4, 1.9, and 8.3 times greater than that of Pt_2Sn–H/NG (256 mA mg_{Pt}^{-1}), Pt_2Sn/NG (197 mA mg_{Pt}^{-1}) and Pt/C (44 mA mg_{Pt}^{-1}), respectively. The high EOR activity of Pt_3Sn@u-SnO_2/NG was further confirmed by the Tafel plots as shown in Fig. 4e. The Tafel slope on Pt_3Sn@u-SnO_2/NG is 284 mV dec^{-1}, much lower than that of commercial Pt/C (319 mV dec^{-1}), indicating that Pt_3Sn@u-SnO_2/NG prepared by our strategy can obviously promote the EOR kinetics on the Pt surface. The very high EOR activity of the Pt_3Sn@u-SnO_2/NG catalyst mainly should be attributed to the unique structure of Pt_3Sn NPs enriched with Pt_3Sn/SnO_2 interfaces, which make the Pt_3Sn@u-SnO_2/NG catalyst one of the most promising EOR catalysts towards the EOR compared with the most recently reported catalysts (Table S5†).

The chronoamperometric technique was firstly applied to monitor the stabilities of different electrocatalysts. As shown in Fig. 4c, the EOR activities on all catalysts running at the potential of 0.7 V gradually decay with time because the generated intermediates like CO poison the active sites of Pt-based catalysts during the ethanol oxidation. The Pt_3Sn@u-SnO_2/NG catalyst achieves higher mass activity in comparison with the Pt_2Sn–H/NG, Pt_2Sn/NG and Pt/C catalysts during a period of 3600 s (Fig. 4d). After operating the reaction for 3600 s, the retained mass activity on the Pt_3Sn@u-SnO_2/NG catalyst is found to be 110 mA mg_{Pt}^{-1} at the potential of 0.7 V, outperforming the Pt_2Sn–H/NG (69 mA mg_{Pt}^{-1}), Pt_2Sn/NG (54 mA mg_{Pt}^{-1}) and Pt/C (11 mA mg_{Pt}^{-1}), respectively. The stability of the Pt_3Sn@u-SnO_2/NG catalyst was further investigated by the accelerated durability tests (ADTs). The Pt_3Sn@u-SnO_2/NG catalyst retains the highest proportion of its initial activity among all catalysts after 1000 cycles (Fig. 4f and S6†). The Pt_3Sn@u-SnO_2/NG catalyst exhibits superior long-term stability with the loss of 24% of its initial activity, which is about 2.7 times higher than that of the Pt/C catalyst (65%). The Pt_3Sn@u-SnO_2/NG did not show significant agglomeration, and the ultra-small SnO_2 around Pt_3Sn NPs was still visible (Fig. S7†). These findings indicate that the Pt_3Sn@u-SnO_2/NG catalyst possesses excellent performance due to the formation of the interfacial Pt_3Sn–SnO_2 structures on Pt_3Sn NPs.

In addition to the high EOR activity, the Pt_3Sn@u-SnO_2/NG catalyst also shows excellent performance for methanol oxidation as shown in Fig. 5 and Table S6.† The Pt_3Sn@u-SnO_2/NG catalyst has higher MOR peak activity compared with the Pt_2Sn–H/NG, Pt_2Sn/NG and Pt/C catalysts (Fig. 5a). Pt_3Sn@u-SnO_2/NG is found to have higher MOR activity compared with the other samples during 0.45–0.7 V *vs.* RHE (Fig. S8†). Besides the main oxidation peak at about 0.84 V for the MOR, a shoulder peak at 0.72 V was observed for the methanol oxidation reaction, attributed to the different types of active sites for methanol oxidation.[45] As shown in Fig. 5b, the mass activity of the MOR on

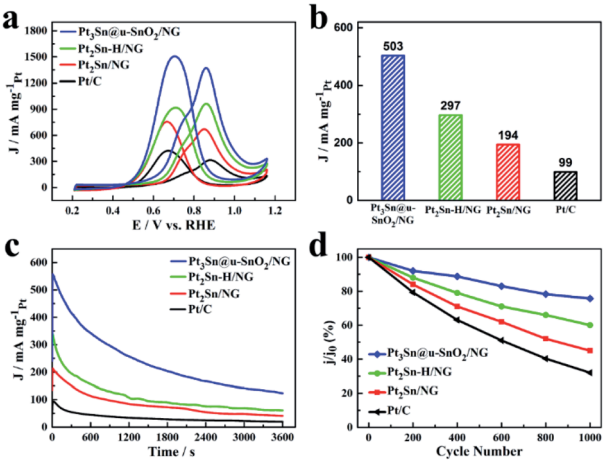

Fig. 5 (a) CV curves of different catalysts in 0.5 M H_2SO_4 + 1 M CH_3OH solution with a sweep rate of 50 mV s^{-1}. (b) The current density of different catalysts at 0.7 V in 0.5 M H_2SO_4 + 1 M CH_3OH solution. (c) Chronoamperometric curves of different catalysts in N_2-saturated 0.5 M H_2SO_4 + 1 M CH_3OH solution at constant voltage 0.7 V for 3600 s. (d) Changes of peak current densities of the MOR during potential cycling of different catalysts.

the Pt_3Sn@u-SnO_2/NG catalyst is 503 mA mg_{Pt}^{-1} at the potential of 0.7 V, outperforming Pt_2Sn–H/NG (297 mA mg_{Pt}^{-1}), Pt_2Sn/NG (194 mA mg_{Pt}^{-1}) and Pt/C (99 mA mg_{Pt}^{-1}), respectively. The MOR mass activity on the Pt_3Sn@u-SnO_2/NG catalyst is 5.1 times higher than that of the Pt/C catalyst. The excellent MOR activity of Pt_3Sn@u-SnO_2/NG was also supported by the Tafel plots (Fig. S9†). The chronoamperometric measurements (Fig. 5c) show that the Pt_3Sn@u-SnO_2/NG catalyst has higher current density and lower current decay in comparison with the other samples, indicating the high stability of the Pt_3Sn@u-SnO_2/NG catalyst for methanol oxidation. The high stability of the Pt_3Sn@u-SnO_2/NG catalyst during the MOR is also confirmed by the ADTs. After ADT (Fig. 5d, S10 and S11†), the Pt_3Sn@u-SnO_2/NG catalyst losses only 25% of its initial activity while the activity of the Pt/C catalyst decreases by 68% under the same operating conditions.

The ability of the CO tolerance on different catalysts was evaluated by CO stripping voltammograms as shown in Fig. 6. It is obvious that the onset potential for CO oxidation on the Pt_3Sn@u-SnO_2/NG catalyst is 0.36 V, lower than that of Pt_2Sn–H/NG (0.55 V), Pt_2Sn/NG (0.64 V) and Pt/C (0.81 V), respectively. The lowest onset potential of Pt_3Sn@u-SnO_2/NG (0.36 V) should be ascribed to the unique structure of Pt_3Sn decorated with ultra-small SnO_2, helping the CO oxidation on the Pt surface at relatively low potentials by the bifunctional effects. Furthermore, the main peak of CO oxidation on the Pt_3Sn@u-SnO_2/NG catalyst has the lowest potential of 0.73 V compared with the other catalysts. This result indicates that the Pt_3Sn@u-SnO_2/NG catalyst possesses high CO tolerance.

The enhanced activity and stability of the Pt_3Sn@u-SnO_2/NG catalyst may be related to the unique structure of Pt_3Sn NPs enriched with Pt_3Sn/SnO_2 interfaces. The Pt_3Sn NPs not only possesses high activity but also stability during the MOR and

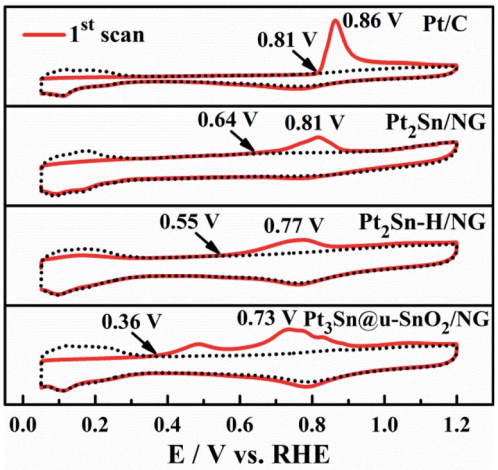

Fig. 6 CO stripping patterns recorded on Pt_2Sn/NG, Pt_2Sn–H/NG, Pt_3Sn@u-SnO_2/NG and Pt/C in 0.5 M H_2SO_4.

EOR process. The incorporation of Sn into Pt lattices is believed to not only tune the Pt electronic structure but also increase the Pt–Pt distance, which results in the enhanced performance for alcohol oxidation by inhibiting CO adsorption and lowering the CO affinity on Pt active sites.[46] Furthermore, the surface decorated ultra-small SnO_2 can generate OH species at low potentials, which can improve the kinetics of CO electro-oxidation on the Pt NPs.

3. Conclusion

In conclusion, we have successfully synthesized Pt_3Sn NPs enriched with Pt_3Sn/SnO_2 interfaces on NG through thermal treatment of Pt_2Sn/NG in a H_2 atmosphere, followed by annealing under H_2 and air conditions. The Pt_3Sn@u-SnO_2/NG catalyst exhibits superior mass activities of 366 mA mg_{Pt}^{-1} for the EOR and 503 mA mg_{Pt}^{-1} for the MOR at 0.7 V, which are 8.3 and 5.1 times better than those of commercial Pt/C, respectively. CO-stripping profiles obtained on the Pt_3Sn@u-SnO_2/NG catalyst showed higher CO tolerance in comparison with Pt/C. The outstanding performance of Pt_3Sn@u-SnO_2/NG catalysts should be ascribed to the synergetic effect induced by the unique structure of Pt_3Sn NPs enriched with Pt_3Sn/SnO_2 interfaces.

4. Methods

4.1 Chemicals

All chemicals were utilized as received without further purification. Chloroplatinic acid hexahydrate [$H_2PtCl_6 \cdot 6H_2O$], tin(II) chloride dehydrate [$SnCl_2 \cdot 2H_2O$], urea [$CO(NH_2)_2$] and ethylene glycol (EG) were of analytical reagent (A.R.) grade and purchased from Sinopharm Chemical Reagent Co., Ltd. Commercial 30 wt% Pt/C was purchased from Johnson Matthey. Deionized water (DI water, Millipore, 18.2 MΩ at 25 °C) was used in all processes.

4.2 Synthesis of the Pt_3Sn@u-SnO_2/NG

The N-doped GO (NG) was synthesized by pyrolysis of the mixture of graphene oxide (GO) prepared by a modified Hummers method[47] and urea in an N_2 atmosphere at 600 °C for 30 minutes. Pt_2Sn/NG was prepared using $SnCl_2 \cdot 2H_2O$ and $H_2PtCl_6 \cdot 6H_2O$ as precursors with the Sn/Pt atomic ratio of 1 : 2 by the polyol method.[39] The Pt_2Sn–H/NG catalyst was obtained by direct heat treatment of Pt_2Sn/NG at 300 °C for 1 h in a 10% H_2/90% N_2 atmosphere. The Pt_3Sn@u-SnO_2/NG catalyst was obtained by direct heat treatment of Pt_2Sn–H/NG at 300 °C for 1 h in an air atmosphere. The Pt loading on Pt_3Sn@u-SnO_2/NG, Pt_2Sn–H/NG and Pt_2Sn/NG catalysts was 14.5 wt%, 16.2 wt% and 15.8 wt%, respectively according to the ICP test.

4.3 Material characterization and electrochemical measurements

The composition, structure and morphology of the prepared catalysts were investigated by transmission electron microscopy (TEM, TECNAL G2F2O) and X-ray powder diffraction (XRD, ULTIMA III). X-ray photoelectron spectroscopy (XPS) spectra were studied with a K-Alpha spectrometer. The Pt loading was obtained using an Inductively Coupled Plasma Mass Spectrometer (ICP-MS) (iCAP7000, Thermo Fisher Scientific). Electrochemical measurements were performed with an Autolab electrochemistry station using a standard three-electrode cell at 25 °C. More detailed information regarding electrochemical testing is provided in the ESI.†

Conflicts of interest

There are no conflicts to declare.

Acknowledgements

This work was supported by the National Natural Science Foundation of China (Grant No. 21875039), Minjiang Professorship (XRC-1677), and Fujian Province's High Level Innovative and Entrepreneurial Talents (50012709).

References

1 R. Chang, L. Zheng, C. Wang, D. Yang, G. Zhang and S. Sun, *Appl. Catal., B*, 2017, **211**, 205–211.
2 J. Bai, D. Liu, J. Yang and Y. Chen, *ChemSusChem*, 2019, **12**, 2117–2132.
3 R. Rizo, S. Pérez-Rodríguez and G. García, *ChemElectroChem*, 2019, **6**, 4725–4738.
4 X. Yue, Y. Pu, W. Zhang, T. Zhang and W. Gao, *J. Energy Chem.*, 2020, **49**, 275–282.
5 X. L. Tian, L. Wang, P. Deng, Y. Chen and B. Y. Xia, *J. Energy Chem.*, 2017, **26**, 1067–1076.
6 Y. Zheng, X. Wan, X. Cheng, K. Cheng, Z. Dai and Z. Liu, *Catalysts*, 2020, **10**, 166.
7 G. L. Zhang, Z. Z. Yang, C. D. Huang, W. Zhang and Y. X. Wang, *Nanoscale*, 2015, **7**, 10170–10177.

8 S. Xue, W. Deng, F. Yang, J. Yang, I. S. Amiinu, D. He, H. Tang and S. Mu, *ACS Catal.*, 2018, **8**, 7578–7584.
9 X. Wang, M. Sun, S. Xiang, M. Waqas, Y. Fan, J. Zhong, K. Huang, W. Chen, L. Liu and J. Yang, *Electrochim. Acta*, 2020, **337**, 135742.
10 Z. Xia, X. Zhang, H. Sun, S. Wang and G. Sun, *Nano Energy*, 2019, **65**, 104048.
11 J. Li, S. Z. Jilani, H. Lin, X. Liu, K. Wei, Y. Jia, P. Zhang, M. Chi, Y. J. Tong, Z. Xi and S. Sun, *Angew. Chem., Int. Ed.*, 2019, **131**, 11651–11657.
12 H. Liu, J. Li, L. Wang, Y. Tang, B. Y. Xia and Y. Chen, *Nano Res.*, 2017, **10**, 3324–3332.
13 S. Yin, Z. Wang, X. Qian, D. Yang, Y. Xu, X. Li, L. Wang and H. Wang, *ACS Sustainable Chem. Eng.*, 2019, **7**, 7960–7968.
14 S. Dai, T.-H. Huang, X. Yan, C.-Y. Yang, T.-Y. Chen, J.-H. Wang, X. Pan and K.-W. Wang, *ACS Energy Lett.*, 2018, **3**, 2550–2557.
15 Q. Lu, J. Huang, C. Han, L. Sun and X. Yang, *Electrochim. Acta*, 2018, **266**, 305–311.
16 Y. Zhang, F. Gao, T. Song, C. Wang, C. Chen and Y. Du, *Nanoscale*, 2019, **11**, 15561–15566.
17 J. Bai, X. Xiao, Y. Y. Xue, J. X. Jiang, J. H. Zeng, X. F. Li and Y. Chen, *ACS Appl. Mater. Interfaces*, 2018, **10**, 19755–19763.
18 S. Yin, R. D. Kumar, H. Yu, C. Li, Z. Wang, Y. Xu, X. Li, L. Wang and H. Wang, *ACS Sustainable Chem. Eng.*, 2019, **7**, 14867–14873.
19 Y. Bao, F. Wang, X. Gu and L. Feng, *Nanoscale*, 2019, **11**, 18866–18873.
20 L. Yang, J. J. Ge, C. P. Liu, G. L. Wang and W. Xing, *Curr. Opin. Electrochem.*, 2017, **4**, 83–88.
21 L. Zheng, D. Yang, R. Chang, C. Wang, G. Zhang and S. Sun, *Nanoscale*, 2017, **9**, 8918–8924.
22 F. Zhao, Q. Yuan, B. Luo, C. Li, F. Yang, X. Yang and Z. Zhou, *Sci. China Mater.*, 2019, **62**, 1877–1887.
23 M. Roca-Ayats, O. Guillén-Villafuerte, G. García, M. Soler-Vicedo, E. Pastor and M. V. Martínez-Huerta, *Appl. Catal., B*, 2018, **237**, 382–391.
24 Y. Ma, H. Wang, S. Ji, V. Linkov and R. Wang, *J. Power Sources*, 2014, **247**, 142–150.
25 F. Wu, D. Zhang, M. Peng, Z. Yu, X. Wang, G. Guo and Y. Sun, *Angew. Chem., Int. Ed.*, 2016, **55**, 4952–4956.
26 J. Yu, M. Jia, T. Dai, F. Qin and Y. Zhao, *J. Solid State Electrochem.*, 2016, **21**, 967–974.
27 H. Sun, Y. Lian, C. Yang, L. Xiong, P. Qi, Q. Mu, X. Zhao, J. Guo, Z. Deng and Y. Peng, *Energy Environ. Sci.*, 2018, **11**, 2363–2371.
28 M. Chen, Y. Han, T. W. Goh, R. Sun, R. V. Maligal-Ganesh, Y. Pei, C. K. Tsung, J. W. Evans and W. Huang, *Nanoscale*, 2019, **11**, 5336–5345.
29 W. Chen, Z. Lei, T. Zeng, L. Wang, N. Cheng, Y. Tan and S. Mu, *Nanoscale*, 2019, **11**, 19895–19902.
30 Y. Uemura, Y. Inada, K. K. Bando, T. Sasaki, N. Kamiuchi, K. Eguchi, A. Yagishita, M. Nomura, M. Tada and Y. Iwasawa, *Phys. Chem. Chem. Phys.*, 2011, **13**, 15833–15844.
31 J. W. Magee, W.-P. Zhou and M. G. White, *Appl. Catal., B*, 2014, **152–153**, 397–402.
32 L. Zheng, S. Zheng, Z. Zhu, Q. Xu, G. Zhang, S. Sun and D. Yang, *Adv. Mater. Interfaces*, 2018, **5**, 1800748.
33 Z. Yang, M. Li, P. Cui, G. Zhang, X. Jiang and Y. Wang, *ACS Sustainable Chem. Eng.*, 2018, **6**, 14026–14032.
34 Z.-Y. Li, J. Zhou, L.-S. Tang, X.-P. Fu, H. Wei, M. Xue, Y.-L. Zhao, C.-J. Jia, X.-M. Li, H.-B. Chu and Y. Li, *J. Mater. Chem. A*, 2018, **6**, 2318–2326.
35 G. Yang, A. I. Frenkel, D. Su and X. Teng, *ChemCatChem*, 2016, **8**, 2876–2880.
36 Y. Qu, Y. Gao, L. Wang, J. Rao and G. Yin, *Chem.–Eur. J.*, 2016, **22**, 193–198.
37 X. Fan, M. Tang, X. Wu, S. Luo, W. Chen, X. Song and Z. Quan, *J. Mater. Chem. A*, 2019, **7**, 27377–27382.
38 L. Wang, W. Wu, Z. Lei, T. Zeng, Y. Tan, N. Cheng and X. Sun, *J. Mater. Chem. A*, 2020, **8**, 592–598.
39 L. Jiang, G. Sun, Z. Zhou, W. Zhou and Q. Xin, *Catal. Today*, 2004, **93–95**, 665–670.
40 C. Chen, H. Xu, H. Shang, L. Jin, T. Song, C. Wang, F. Gao, Y. Zhang and Y. Du, *Nanoscale*, 2019, **11**, 20090–20095.
41 W. Du, G. Yang, E. Wong, N. A. Deskins, A. I. Frenkel, D. Su and X. Teng, *J. Am. Chem. Soc.*, 2014, **136**, 10862–10865.
42 J. Zhu, X. Zheng, J. Wang, Z. Wu, L. Han, R. Lin, H. L. Xin and D. Wang, *J. Mater. Chem. A*, 2015, **3**, 22129–22135.
43 W. Chen, Z. Lei, T. Zeng, L. Wang, N. Cheng, Y. Tan and S. Mu, *Nanoscale*, 2019, **11**, 19895–19902.
44 F. J. Rodríguez Varela and O. Savadogo, *J. Electrochem. Soc.*, 2008, **155**, B618–B624.
45 L. Ma, X. Zhao, F. Si, C. Liu, J. Liao, L. Liang and W. Xing, *Electrochim. Acta*, 2010, **55**, 9105–9112.
46 J. Shim, J. Lee, Y. Ye, J. Hwang, S. K. Kim, T. H. Lim, U. Wiesner and J. Lee, *ACS Nano*, 2012, **6**, 6870–6881.
47 N. C. Cheng, J. Liu, M. N. Banis, D. S. Geng, R. Y. Li, S. Y. Ye, S. Knights and X. L. Sun, *Int. J. Hydrogen Energy*, 2014, **39**, 15967–15974.